Available online at www.sciencedirect.com
SCIENCE DIRECT®
Aerospace Science and Technology 7 (2003) 532–539
Aerospace Science and Technology
www.elsevier.com/locate/aescte

An efficient aerodynamic boundary element method for aeroelastic simulations and its experimental validation

David Eller *, Martin Carlsson

Department of Aeronautics, Kungliga Tekniska Högskolan, SE-100 44 Stockholm, Sweden

Received 18 September 2002; received in revised form 12 March 2003; accepted 23 June 2003

Abstract

An unstructured aerodynamic boundary element method employing panel clustering and iterative solution techniques for efficiency has been implemented. The solver is used in unsteady coupled simulations including applications in subsonic aeroelasticity. In comparison to existing linear methods, it allows more consistent modeling of complex three-dimensional geometries without requiring excessive mesh generation and computational effort. Due to a time-domain approach, simulations involving nonlinear structures or flight dynamics can be performed. A dynamic aeroelastic validation experiment is presented which shows that the solver predicts highly transient, damped aeroelastic motion with good accuracy.

Zusammenfassung

Für Anwendungen in instationären gekoppelten Simulationen wurde eine aerodynamische Randelementmethode implementiert. Im Vergleich zu vorhandenen Programmen weist der Löser dank der Verwendung unstrukturierter Oberflächennetze, Panel-clustering und iterativer Lösungsalgorithmen mehr Flexibilität bei der Geometriemodellierung sowie ein signifikant besseres Skalierungsverhalten auf. Zu Validierungszwecken wurden Berechnungsergebnisse mit dynamischen aeroelastischen Deformationsmessungen an einem Windkanalmodell verglichen, wobei festgestellt werden konnte, dass die entwickelte Randelementmethode die transiente, gedämpfte Bewegung mit hoher Genauigkeit vorhersagt.

Keywords: Aeroelasticity; Boundary elements; Unstructured mesh

Schlüsselwörter: Aeroelastizität; Randelemente; Unstrukturiertes Netz

1. Introduction

For numerical investigations of coupled problems involving unsteady aerodynamics, several different approaches with vastly varying complexity and computational cost have been followed in the past. Frequency domain methods such as the Doublet Lattice Method (Albano and Rodden [1]) are very efficient in predicting aeroelastic stability boundaries in subsonic flow, using linear structural models. The doublet lattice method represents lifting surfaces as thin panels, which makes it difficult to use in cases where the actual geometry cannot reasonably be approximated as a flat plate. Fluid displacement effects, which can be relevant for e.g. airship applications, are also neglected. Moreover, as the DLM is a frequency-domain method, it cannot easily be coupled with nonlinear structural or flight dynamics analysis.

On the other end of the spectrum, research in the field of unsteady Euler and Reynolds-averaged Navier–Stokes solvers for aeroelastic computations is very active. Some current approaches are based on unstructured meshes (Farhat et al. [9], Slone et al. [21], Degand and Farhat [6], Fornasier et al. [10]). Other, especially those including viscous effects, employ block structured grids (Meijer and Prananta [17], Henke [12], Zwaan and Prananta [22]). While these methods incorporate the best available physical flow models, their cost in terms of simulation setup, mesh handling and computation times for complex three-dimensional cases is still high. This is certainly acceptable for large and expensive projects such as the certification of fighter aircraft [7],

* Corresponding author.
E-mail addresses: dlr@kth.se (D. Eller), martinc@kth.se (M. Carlsson).

1270-9638/$ – see front matter
doi:10.1016/S1270-9638(03)00056-7

but for design, when fast turnaround times become paramount, unsteady high fidelity field methods are too expensive.

Linear panel methods, which require a surface mesh only, tend to be less demanding in terms of computational resources and thus seem a good choice for the application in mind. Existing codes, however, need structured grids and do not scale well for complex geometries [2,14]. In addition, not all programs were designed for unsteady coupling, making substantial modifications necessary.

A new aerodynamic boundary element method has therefore been implemented in order to achieve sufficient geometric modeling realism with moderate mesh generation and computational effort. It is intended to be used in time domain simulations of problems where unsteady subsonic aerodynamics couple strongly with (possibly geometrically nonlinear) structural elasticity, flight dynamics and flight control systems. Some of these coupled problems cannot be treated in the frequency domain. Examples of possible future applications are the computation of deformations and loads for elastic aircraft such as high altitude, long endurance UAV or glider aircraft, or the prediction of maneuver characteristics of such configurations. Since complex three-dimensional geometries need to be handled, unstructured surface meshes are used to reduce the modeling effort.

In the following, the aerodynamic solver is described in some detail, including implementation aspects. Then, computations for a simple case of a wing in pitching motion are compared to results from the well-known Doublet Lattice Method. Finally, an aeroelastic validation experiment, performed in order to investigate the accuracy of the aerodynamics code, is documented and followed by a comparison with computational results.

2. Numerical modeling

The numerical method employed solves the linearized potential flow equations in boundary integral form. Therefore, only the surface of the body needs to be discretized, which is an important advantage for unsteady simulations where both flow field and surface shape change in time. Unsteady methods using domain discretizations must employ some form of field mesh deformation process which can become rather involved [6].

Because the method is based on linear potential flow, it is naturally limited with respect to the physical phenomena which can be accurately represented. Large regions of separated flow, very high alpha maneuvers and shock flows can clearly not be modeled with any reasonable fidelity. However, flow separation is a viscous effect which needs some time to fully develop, so that potential flow methods are often more accurate in predicting unsteady pressures than what would be expected from steady calculations [14].

2.1. Boundary element method

As a boundary integral method, the current implementation uses a distribution of singular kernel functions fulfilling the Laplace equation for the velocity potential Φ according to

$$\nabla^2 \Phi = 0. \tag{1}$$

The function coefficients are obtained by solving a set of equations resulting from the boundary conditions in inner Dirichlet form. Expressing the potential at some point $\mathbf{x}$ as the sum of a known freestream potential Φ_∞ and a disturbance potential Φ^* induced by the body, Lamb [16] states that the disturbance potential must be constant at any point $\mathbf{x}_i$ on the inside surface S of an impermeable body,

$$\Phi(\mathbf{x}) = \Phi_\infty(\mathbf{x}) + \Phi^*(\mathbf{x}), \tag{2}$$

$$\Phi^*(\mathbf{x}_i) = \text{const} \quad \text{for } \mathbf{x}_i \text{ on } S. \tag{3}$$

This formulation is commonly used in traditional panel methods because surface velocities can be obtained relatively efficiently. Assuming a distribution of source and doublet singularities on the surface, the disturbance potential can be expressed as

$$\begin{aligned} 4\pi \Phi^*(\mathbf{x}_i) = 4\pi K_i \mu_{s,i} &+ \int_S \frac{\mathbf{n}^{\mathrm{T}}(\mathbf{x}_i - \mathbf{x})}{|\mathbf{x}_i - \mathbf{x}|^3} \mu_x \,\mathrm{d}S_s \\ &+ \int_W \frac{\mathbf{n}^{\mathrm{T}}(\mathbf{x}_i - \mathbf{x})}{|\mathbf{x}_i - \mathbf{x}|^3} \mu_w \,\mathrm{d}S_w \\ &- \int_S \frac{\sigma}{|\mathbf{x}_i - \mathbf{x}|} \,\mathrm{d}S_s, \end{aligned} \tag{4}$$

where μ are doublet distributions on the body surface (index s) or wake (index w) and σ represents a source distribution. Moreover, $\mathbf{x}_i$ designates an interior collocation point on the surface, and K_i the doublet self-influence coefficient, while $\mathbf{x}$ and $\mathbf{n}$ are position and local outward normal vector of the surface S.

In contrast to most conventional codes, the body surface is discretized using flat triangular elements carrying a piecewise linear distribution of source and doublet strengths. Triangular boundary elements can be obtained from a fully automatic surface triangulation procedure, whereas a structured surface mesh can require significant additional effort, especially in the case of large and intricate geometrical configurations [8]. Further, linear instead of the usually element-wise constant singularity distributions allow better pressure resolution in regions of strong doublet gradients.

At the trailing edge of lifting surfaces, the vortex wake is modeled by a thin doublet sheet, which is discretized in the same manner as the body surface. Doublet strengths in the wake are obtained from a discrete form of the empirical Kutta condition in velocity form, stating that the velocity component normal to the trailing edge must vanish:

$$\mathbf{n}_{te}^{\mathrm{T}}(\nabla \Phi_\infty + \nabla \Phi^*) = \mathbf{n}_{te}^{\mathrm{T}}(\mathbf{v}_\infty - \nabla \mu_s) = 0. \tag{5}$$

Here, $\mathbf{n}_{te}$ is a vector normal to the trailing edge, $\mathbf{v}_\infty$ the freestream velocity at the trailing edge and μ_s the local doublet strength. A drawback of this form is that blunt trailing edges cannot easily be treated.

The current implementation allows the treatment of flexible wakes, meaning that the wake surface is deformed so that it is parallel to the flow everywhere. This procedure can be quite expensive since field velocities need to be computed at every wake vertex, but ensures that the wake surface is completely free of force.

Discretizing the integral equation (4) obtained from the Dirichlet boundary conditions by the collocation method leads to n_v equations for the unknown surface doublet strengths, where n_v is the number of mesh vertices. The n_v source strengths σ are computed by an approximate form [14], avoiding the solution of an additional system of equations. The Kutta condition provides one equation per trailing edge point for the doublet strength of the wake emanating from that point. Since the number of points n_w lying on wake separation lines is generally relatively small, the additional cost of solving these wake equations is moderate. In unsteady simulations, a new set of trailing edge wake strengths μ_w^n is computed at each time step, while the doublet strengths of the previous steps are convected downstream in the wake surface. The effect of the downstream wake doublets μ_w^o, i.e. all doublet strengths except those corresponding to points on the trailing edges, appears on the right hand side of the linear system.

Combining the equations obtained from the Dirichlet condition and the wake equations results in a blocked linear system

$$\begin{bmatrix} B_s & B_w^n \\ C & 0 \end{bmatrix} \begin{bmatrix} \mu_s \\ \mu_w^n \end{bmatrix} = \begin{bmatrix} r_s \\ r_w \end{bmatrix} \tag{6}$$

which is solved by

$$u = B_s^{-1} r_s, \tag{7}$$

$$v = r_w - Cu, \tag{8}$$

$$F = B_s^{-1} B_w^n, \tag{9}$$

$$\mu_w^n = -(CF)^{-1} v, \tag{10}$$

$$\mu_s = u - F\mu_w^n. \tag{11}$$

The right hand side components r_s and r_w are obtained from the Dirichlet and wake equations, respectively:

$$r_s = A\sigma - B_w^o \mu_w^o, \tag{12}$$

$$r_{w,i} = \mathbf{n}_{te,i}^{\mathrm{T}}, \mathbf{v}_{\infty,i}. \tag{13}$$

The length of r_s is n_v since there is one surface doublet and one source strength per vertex. With one unknown wake doublet strength per trailing edge point, the length of r_w is n_w, which is much less than n_v.

In Eq. (6), the blocks B_s and B_w^n are the surface and wake doublet influence matrices for the trailing edge wake strengths, respectively, while A represents the source singularity influence coefficients. All influence coefficients are obtained from Eq. (4). The rows of matrix C contain the local surface gradient operator left-multiplied by the trailing edge normal vector $\mathbf{n}_{te}$.

For small problems, i.e. up to around 1000 mesh vertices, the resulting linear system is most efficiently solved directly. However, the computational cost and memory requirement of a direct solution grow with at least the square of n_v, restricting analysis to simple geometries or rather coarse discretizations. To overcome this limitation, the current implementation uses a variant of panel clustering (Hackbusch and Nowak [11]) and iterative solution algorithms.

The coefficient matrix of the linear system to be solved consists of influence coefficients obtained by integrating the potential influence of singularity elements on collocation points. The influence, or kernel function, quickly decreases with distance between boundary element and collocation point. Exploiting this, the influence of a group of elements on a whole set of remote collocation points can be computed efficiently using an approximate expansion of the exact kernel function. In this manner, influence coefficients for a model with n_v vertices can be obtained from $\mathrm{O}(n_v \log^2 n_v)$ operations instead of $\mathrm{O}(n_v^2)$. Influence coefficients for collocation points which are not sufficiently separated from the inducing boundary elements are still computed directly and stored in a sparse nearfield matrix. Application of a graph reordering procedure from the Metis library (Karypis and Kumar, [13]) improves both the condition number and sparsity of the nearfield matrix considerably.

Using sparse nearfield and cluster-based farfield influence coefficients, standard iterative algorithms can be applied. For general geometries, the preconditioned Generalized Minimal Residuals method GMRES [3] was found to be efficient. Following the ideas of the mesh-neighbor preconditioner proposed by Chen [5] for dense linear systems, the approximate inverse of the sparse nearfield matrix is used as a preconditioner. This approach succeeds in making the number of GMRES iterations independent of mesh resolution, so that, in most cases, less than ten iterations are required per timestep.

For reasonable discretizations, the iterative procedure using panel clustering is superior to direct solution for geometries of more than about 1000 vertices. Arguably more important than the reduction in computation time is the lower memory requirement which allows fairly large problems to be treated on inexpensive hardware.

2.2. Aeroelastic coupling

While the aerodynamic solver can be used in simulations of different coupled problems, an aeroelastic validation case is presented in Section 5. Therefore, the approach taken to couple the computational aerodynamics with a structural model is described in the following. Neither the structural dynamics model nor the time integration involved is meant to be used for more general, large-scale problems.

A beam-like structural finite element model of an existing Blended Wing Body (BWB) wind tunnel model [4] is available and provides a set of structural eigenmodes. Using a subspace spanned by a few (four to ten) eigenvectors contained in the matrix Z, the equations of motions

$$M\ddot{x} + C\dot{x} + Kx = f_a(t) \tag{14}$$

are transformed into modal coordinates y, leading to

$$Z^{\mathrm{T}}MZ\ddot{y} + Z^{\mathrm{T}}CZ\dot{y} + Z^{\mathrm{T}}KZy = Z^{\mathrm{T}}f_a(t), \quad \text{or} \tag{15}$$

$$\ddot{y} + D\dot{y} + \Omega y = f_z(t), \quad \text{with} \tag{16}$$

$$\Omega = \operatorname{diag}(\omega_i^2) = Z^{\mathrm{T}}KZ \quad \text{and} \tag{17}$$

$$D = \operatorname{diag}(\delta_i) = Z^{\mathrm{T}}CZ \quad \text{since} \tag{18}$$

$$Z^{\mathrm{T}}MZ = I. \tag{19}$$

Here, M, C and K are mass, modal damping and stiffness matrices, respectively, and ω_i is the i^{th} eigenfrequency. In addition, $f_a(t)$ designates the aerodynamic load vector and $f_z(t)$ its projection in the modal subspace. The load vector is built up by integrating surface pressures on the spanwise segments from which the model is constructed [4]. The structural eigenvectors z_i (constituting the columns of Z) are mass-normalized so that

$$z_i^{\mathrm{T}}Mz_i = 1. \tag{20}$$

Replacing $\ddot{y}$ and $\dot{y}$ in (16) by second order finite difference approximations,

$$\dot{y} \approx \frac{y^{k+1} - y^{k-1}}{2\Delta t}, \tag{21}$$

$$\ddot{y} \approx \frac{y^{k+1} - 2y^k + y^{k-1}}{\Delta t^2}, \tag{22}$$

the following explicit time integration scheme is obtained

$$y^{k+1} = \frac{\Delta t^2}{1 + \delta\Delta t}\left(f_z^k + \left(\frac{2}{\Delta t^2} - \omega^2\right)y^k + \left(\frac{\delta}{\Delta t} - \frac{1}{\Delta t^2}\right)y^{k-1}\right) \tag{23}$$

for a discrete timestep Δt. To resolve an eigenmode with good accuracy, at least 20 timesteps per oscillation should be used with this scheme. However, since aeroelastic motion often is dominated by a few low-frequency modes, good overall accuracy can be obtained even if only these eigenmodes are resolved with small timesteps.

Naturally, other time integration schemes should be used for problems where the deformation cannot easily be expressed in terms of structural eigenvectors. However, in the context of the current validation experiment, it proved sufficient because accuracy required a smaller timestep than the stability limit.

From the initial state, the system is allowed to develop a steady wake doublet distribution, which requires about 15 time steps. Then, constraints on the modal deformations are released, allowing the motion to begin.

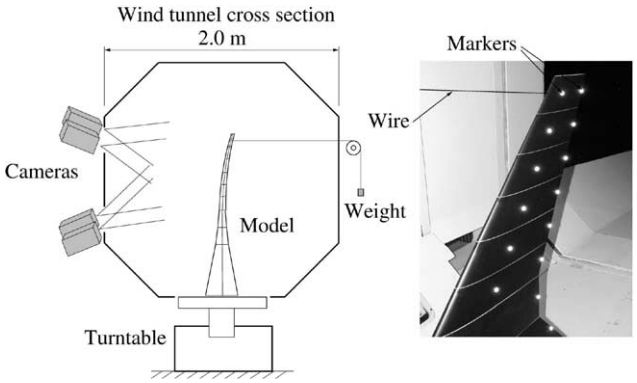

Fig. 1. Experimental setup and locations of the optical markers.

3. Experimental setup

Validation experiments were performed in the low speed wind tunnel L2000 at Kungliga Tekniska Högskolan (KTH). A half span aeroelastic model representing a BWB aircraft served as the test object. The BWB aeroelastic model is further described in [4].

The environmental test conditions were throughout the tests room temperature and atmospheric pressure. Hence, standard sea level atmospheric conditions were used in all conversions between dynamic pressure q_∞ and airspeed v_∞.

The model was rotated to an initial angle of attack $\alpha = 2^\circ$ using a wind tunnel turntable. Then, the wing was initially deflected using a wire arrangement as shown in Fig. 1. The wing was then released from the forced deflection by an electrical release mechanism at the wing tip. This experimental procedure was performed at the three different airspeeds of $v_\infty = 20$, 30 and 40 m s^{-1}.

The motion of the wing was measured using an optical positioning system mounted in the wind tunnel [15,20]. For this purpose, passive reflecting markers were used as targets on the model surface according to Fig. 1. For all three experiments, the wing motion was sampled at 240 Hz. The sampling was initiated before the wing was released from the initial deflected state and interrupted when the wing had stabilized at some static aeroelastic equilibrium. Hence, both the initial deformation and the final deformation were measured during one sampling sequence. The measured elastic deformation refers to the deviation from the reference condition at $\alpha = 2^\circ$ and at $v_\infty = 0$ m s^{-1}.

Using the marker setup shown in Fig. 1, the three-dimensional spatial resolution of the optical system is on the order of 30 μm in the out-of-plane coordinate direction. The torsional deformation is obtained from the difference in out-of-plane displacement between the two chordwise markers at each spanwise coordinate, resulting in a torsional resolution of the order of 0.03°at the wing tip.

A Nastran finite element model of the wing structure was used to obtain a modal model of the structure. In Table 1, eigenfrequencies computed from the Nastran model are compared with experimentally obtained frequencies, showing that the structural model in itself is reasonably accurate.

Table 1
Frequencies and shape classification of the first seven structural eigenmodes

Mode	f_{fem} [Hz]	f_{exp} [Hz]	Shape
1	6.13	6.20	1st bending
2	23.1	22.2	2nd bending
3	36.2	37.9	1st torsion
4	54.6	55.2	2nd torsion
5	63.0	65.7	3rd b. + 2nd t.
6	73.8	81.2	3rd b. + 2nd t.
7	102	98.3	4th b. + 3rd t.

4. Comparison with DLM

In order to investigate the characteristics of the boundary element code for unsteady simulations, calculations for a simple test case have been performed. In order to enable a direct comparison with the frequency-space Doublet Lattice Method, a harmonic rigid body motion in pitch was simulated for the wind tunnel wing configuration as described above.

The boundary element method was used to perform a time domain analysis of a sinusoidal pitching motion with amplitude $\hat{\alpha} = 2°$, for a duration of three oscillations and starting with steady flow. The center of rotation was located at 1.0 m behind the wing apex, i.e. about 12% reference chord behind the aerodynamic center. After less than one period of oscillation, no transient effects were visible in the force history, and the remaining part of the recorded force and moment history were used to obtain amplitude and phase of the corresponding integral coefficients. For use with the DLM, the geometry was modeled as a flat plate discretized with 8 panels chordwise and 24 per semispan. As a frequency-domain method, the DLM provides complex integral coefficients from which amplitude and phase with respect to the prescribed angular motion can be obtained directly.

Fig. 2 shows a comparison of normal force and pitching moment coefficients for a range of reduced frequencies $k = \omega\bar{c}/2u_\infty$ up to 1.5, computed with a reference chord $\bar{c} = 0.75$ m. Amplitudes for $C_{L,\hat{\alpha}}$ and $C_{my,\hat{\alpha}}$ are shown in the upper diagram and phase difference between angle and force in the lower.

At low reduced frequencies, the moment coefficients match well, although the normal force coefficients from the boundary element method are slightly higher. This could be due to a different chordwise pressure distribution caused by the body thickness which the DLM does not account for. Comparison of steady calculations ($k = 0$) with force and moment measurements from [4] for the flexible outboard part of the wind tunnel model shows good agreement with the results obtained here.

While differences in coefficient amplitudes are moderate for reduced frequencies below 0.8, this is no longer the case for faster motion. At $k = 1.5$, the amplitude of both force and moment are predicted considerably higher than with the doublet lattice method. This is probably due to the different formulation of the Kutta condition, which is

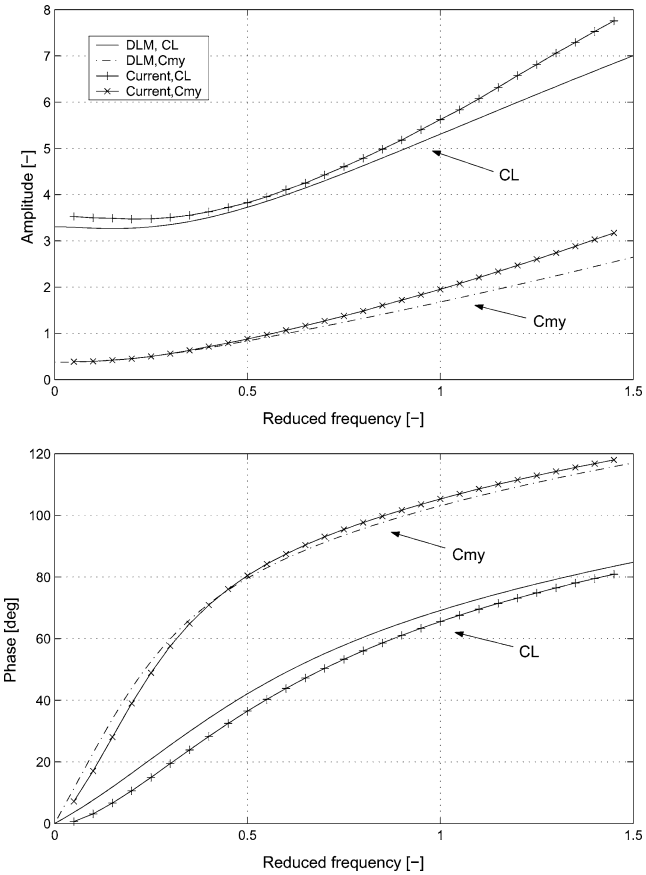

Fig. 2. Amplitude and phase of lift and pitching moment coefficient compared to DLM results, both for $M_\infty = 0.2$.

imposed in velocity form (5) in the current method and differs from the vortex form used in the DLM. Comparing phase differences for current and DLM method, it is noted that while the phase of the moment coefficient differ only slightly, the DLM appears to predict about 5° larger phase lag between force and angle than the current method throughout the frequency range. Again, this is likely a consequence of the dissimilar variants of the Kutta condition used to determine wake doublet strengths. While it is certain that the established DLM does produce the correct phase, the differences observed with the current code do not appear to hinder correct prediction of aeroelastic motion as described in the next section. However, further investigations regarding the effect of the velocity trailing edge condition (5) are necessary.

5. Experimental validation

The experiment described in Section 3 was numerically simulated with a number of different mesh resolutions, time integration steps and modal subspaces. The results presented in the following were obtained with the coarsest mesh used, consisting of 1400 surface triangles per half-model, and the smallest modal subspace of just four eigenmodes. Since

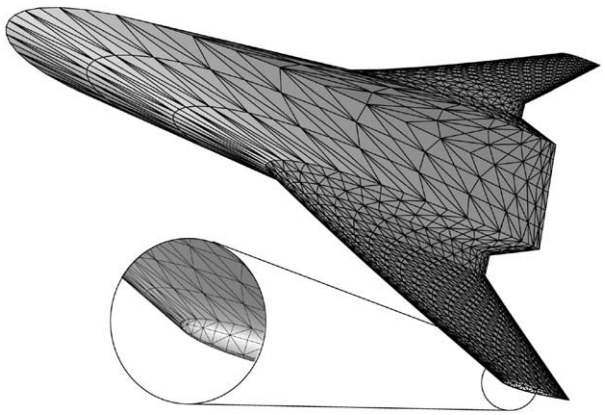

Fig. 3. Computational mesh for the wind tunnel model.

the method presented is meant to be used with limited computational resources and reduced information about structural properties, it is reasonable to emphasize results obtained with such restrictions in place. More computational effort, invested in finer mesh resolution and larger modal subspaces, leads to slightly improved accuracy.

In Fig. 3, the computational mesh is shown. Since the wind tunnel model is constructed from a number of independent trapezoidal segments for each of which pressures need to be integrated separately, the mesh is in this case obtained by triangulating a structured mesh.

Modal damping constants δ_j for this particular structure were not available at the time the simulations were performed. However, for a similar wind tunnel model, measured damping parameters had been found to lie in the neighborhood of only 0.5%. Simulations with structural damping of 1% revealed no significant differences, so that the results shown in the following are those obtained without any structural damping. This is considered reasonable since accurate data on structural damping is often difficult to obtain, especially when hardware is not yet available for vibration testing.

Due to the specific experimental setup used, the wing tip shows the largest motion amplitudes, and its measured and computationally predicted oscillation is therefore discussed here. Figs. 4 and 5 show the deformation time history of the optical marker located closest to the wing tip and at 30% chord. While the top graph in each figure represents the development of bending deflection, the lower shows local twist angle. The highest eigenfrequency involved is that of the fourth mode at 54.6 Hz, which is resolved with twenty timesteps per oscillation.

In order to represent the experiment correctly, the numerical simulation must be started with a fixed initial deformation state in steady flow. This initial deformation state is known from measurements in terms of physical deformation coordinates, but needs to be represented in modal coordinates which are obtained from a weighted least-squares fit minimizing the approximation error. Since the finite element model contains both deflections and angular deformations, some kind of weighting must be employed for the fitting procedure. Here, the fitting error was minimized in terms of point deflection errors. While this approach appears straightforward, it results in fairly low weights for the angular degrees of freedom: Due to the small wing chord, a considerable difference of the torsion angle (e.g. at the tip) results in a small deflection error only. Different weighting schemes can certainly improve this situation, but must rely on rather arbitrary weighting parameters, which should be avoided. Although the fitting of the initial state in modal coordinates thus leads to an error in the initial twist angle at the tip, the deflection history is nevertheless predicted rather accurately and even the development of aeroelastic wing tip twist is captured reasonably well.

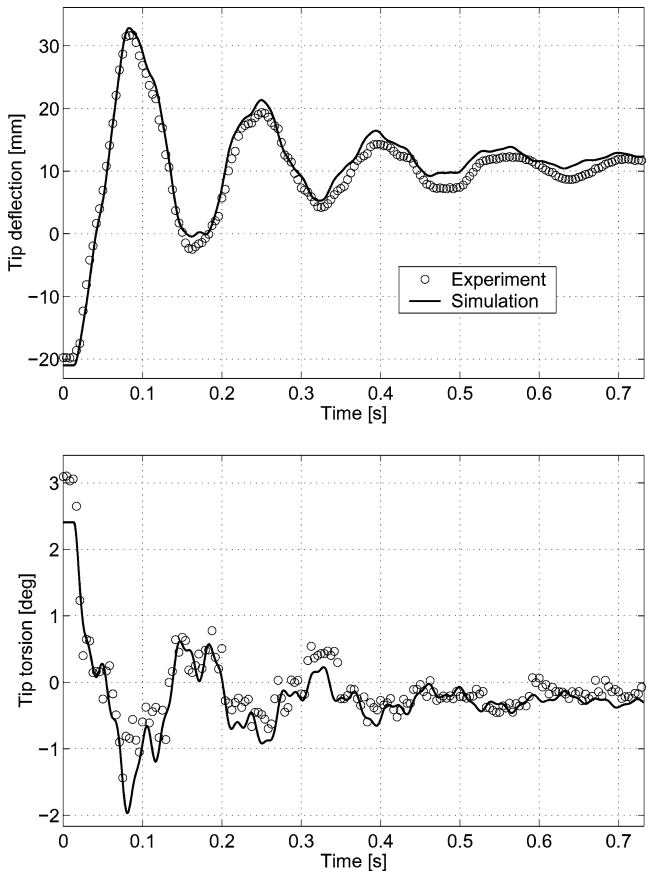

Fig. 4. Wing tip bending deflection and torsion over time for $v_\infty = 20\,\mathrm{m\,s^{-1}}$.

On the other hand, the final equilibrium torsion deformation of the wing tip is computed with relatively low accuracy. Given the fact that the angular deformation even at the tip is smaller than 0.5°, the measurement accuracy may play a role because only relative deformations can be obtained from the optical measurement system. Furthermore, previous steady flow validation experiments with the same configuration have shown that it is difficult to obtain highly accurate twist moments with the current solver implementation, since they are computed as small differences of large pressure values.

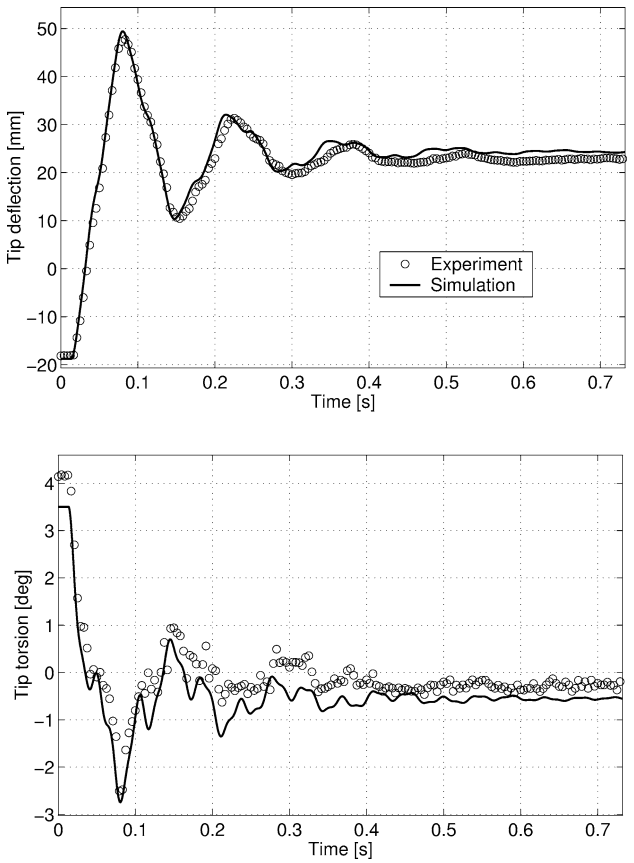

Fig. 5. Wing tip bending deflection and torsion over time for $v_\infty = 30\ \mathrm{m\,s^{-1}}$.

In order to compare simulations with different modal resolution of the structural model and at different freestream velocities, a single scalar measure is presented which characterizes to some extent the damping properties of both experimentally and numerically obtained oscillations. A damping time constant τ is computed as a least-squares fit of a sum of exponentially damped sines to the history of the bending deflection w of the marker on the tip of the wing spar

$$w_m(t) = \sum_{j=1}^{n_f} \hat{w}_j \mathrm{e}^{-t/\tau_j} \sin(\omega_j t + \phi_j) + w_{0,j}. \tag{24}$$

Here, $\hat{w}$ represents the amplitude of oscillation, ω and ϕ the angular frequency and phase shift, and w_0 the static offset reached after the oscillation has been damped out. With more than $n_f = 3$ terms in the sum, no further reduction of the fitting error could be observed. For the cases presented here, the fitting error $|w_m(t_i) - w_i|/|w_i|$ is approximately 1%.

In Table 2, damping constants for experimental data and simulations with varying number of structural eigenmodes (4, 7 and 10) are listed, along with the relative differences $\varepsilon_n = (\tau_n - \tau_{\mathrm{exp}})/\tau_{\mathrm{exp}}$ between simulation and experiment values for three different freestream velocities. Corresponding reduced frequencies with respect to the first structural eigenmode are in the range 0.36 to 0.72. All damping values are those for the first and dominating term in the expansion (24).

Table 2
Damping time constants in milliseconds and differences between least-square fits to experimental and numerical deflection histories

	$20\ \mathrm{m\,s^{-1}}$	$30\ \mathrm{m\,s^{-1}}$	$40\ \mathrm{m\,s^{-1}}$
τ_{exp}	200.4	120.9	95.51
τ_{10}	194.6	124.1	87.73
τ_7	193.4	123.8	88.08
τ_4	190.2	122.0	86.06
ε_{10}	−2.9%	2.6%	−8.1%
ε_7	−3.5%	2.4%	−7.8%
ε_4	−5.1%	0.9%	−9.9%

While damping for the case with $v_\infty = 30\ \mathrm{m\,s^{-1}}$ is slightly weaker than in the experiment, it is stronger in the two other cases. At first, the data in Table 2 may appear to suggest that the inclusion of additional eigenmodes in the modal subspace does not consistently improve accuracy. However, for the first case, where the error is largest, an improvement is achieved. The reason could be that the additionally included modes only in this case participate to a significant degree in the aeroelastic motion. Considering the differences in fitted damping values in comparison to the curve fitting error, it is concluded that the current method predicts the damping properties of the aeroelastic system fairly well.

Further investigations involved finer meshes as well as different timesteps. When comparing the accuracy of deflection history alone, higher mesh resolution does not seem reasonable since its influence is marginal for the current configuration. However, when the chordwise pressure distribution becomes more important, e.g. for wings with control surfaces or if angular deformations must be predicted with high precision, finer spatial discretization will be necessary.

The relative size of the timestep has a significant influence on the accuracy of the time integration scheme (23). When as few as eight steps per period of the highest structural eigenfrequency are used, the motion of the corresponding eigenmode is predicted with reduced precision. Since (23) in itself is second-order accurate, it appears therefore sensible to include as few eigenmodes as reasonably possible, but resolve these modes with twenty steps per oscillation.

For small timesteps, the wake surface consists of a large number of elements, making the computation of local velocities at all vertices for the wake deformation procedure rather expensive. Since, for the case documented here, the difference between flexible and rigid wake formulation was marginal, most simulations were performed with a rigid wake, meaning that the wake surface followed the motion of the trailing edge only, neglecting the effect of induced velocities on the wake shape.

The simulations described above required about 11 s processor time per timestep on a 1.4 GHz Athlon computer. Until now, no serious efforts have been invested in perfor-

mance optimizations other than the reduction of algorithmic complexity by means of the panel clustering method. With finer mesh resolution, the computation time per step increases with $O(n_v \log^2 n_v)$, as expected from implementation properties.

6. Conclusions

As shown by the validation experiment, the developed potential flow solver is capable of performing time domain dynamic aeroelastic analysis with good accuracy, even with constraints on spatial and temporal resolution. Processor time and memory requirements are low and grow significantly slower with mesh size than for conventional panel methods. In combination with automatically generated unstructured surface meshes, this allows credible unsteady analyzes involving geometrically complex configurations at reasonable cost.

In the case of non-linear structures, the time integration can no longer be performed in modal subspace, so that the frequency content of the structural response is no longer known and limited. Use of the current integration would then require excessively small time steps for stability and accuracy; hence a more robust scheme such as implicit Newmark integration [19] or its more general form as proposed by Modak and Sotelino [18] would be advantageous.

Experience from integrating flow solver and structural model showed that non-matching representations (structural beam and aerodynamic surface) account for a major part of the implementation cost. Therefore, matching model types (surface–surface) appear attractive for future efforts.

Object-oriented programming techniques used in the flow solver allowed a straightforward construction of the coupled simulation model and cut implementation efforts considerably.

Acknowledgements

Financial support for this project was provided by the Swedish Research Council (VR) and the Swedish National Program for Aeronautics Research (NFFP). The wind tunnel model used was developed within the project Multi-Disciplinary Design and Optimization for Blended Wing Body Configuration (MOB), financially supported by the Commission of the European Union. Contract number: G4RD-CT1999-0172.

References

[1] E. Albano, W.P. Rodden, A doublet-lattice method for calculationg the lift distribution on oscillating surfaces in subsonic flow, AIAA J. 2 (7) (1969) 279–285.

[2] D.L. Ashby, Potential theory and operation guide for the panel code PMARC 14, Technical Report TM1999-209582, NASA, December 1999.

[3] R. Barrett, M. Berry, T.F. Chan, J. Demmel, J. Donate, J. Dongarra, V. Eijkhout, R. Pozo, C. Romine, H. Van der Vorst, Templates for the Solution of Linear Systems: Building Blocks for Iterative Methods, SIAM Publications, 1994.

[4] M. Carlsson and J. Kuttenkeuler, Design and testing of a blended wing body aeroelastic wind tunnel model, Technical Report, Department of Aeronautics, Report 2002-8, Royal Institute of Technology, Stockholm, 2002.

[5] K. Chen, On a class of preconditioning methods for dense linear systems from boundary element methods, SIAM J. Scientific Comput. 20 (2) (1998) 684–698.

[6] C. Degand, C. Farhat, A three-dimensional torsional spring analogy method for unstructured dynamic meshes, Computers and Structures 80 (2002) 305–316.

[7] B.J.G. Eussen, M.H.L. Hounjet, J.J. Meijer, B.B. Prananta, and I.W. Tjatra, Perspectives of NLR aeroelastic methods to predict wing/store flutter and dynamic loads of fighter-type aircraft, Technical Report NLR-TP-2000-477, NLR, Amsterdam, September 2000.

[8] B.J.G. Eussen, M.H.L. Hounjet, R.J. Zwaan, Experiences in aeroelastic simulation practices, Technical Report NLR-TP-96591, NLR, Amsterdam, September 1996.

[9] C. Farhat, P. Geuzaine, G. Brown, Application of a three-field nonlinear fluid structure formulation to the prediction of the aeroelastic parameters of an F-16 fighter, Computers and Fluids 32 (2002) 3–29.

[10] L. Fornasier, H. Rieger, U. Tremel, E. van der Weide, Time-dependent aeroelastic simulation of rapid maneuvering aircraft, in: 40th AIAA Aerospace Sciences Meeting and Exhibit, 2002. AIAA paper 2002-0949.

[11] W. Hackbusch, Z.P. Nowak, On the fast matrix multiplication in the boundary element method by panel clustering, Numer. Math. 54 (4) (1989) 463–491.

[12] H.H. Henke, The viscous-coupled 3D Euler method EUVISC and its aeroelastic application, in: International Forum for Aeroelasticity and Structural Dynamics, Vol. II, Madrid, 2001, pp. 95–106.

[13] G. Karypis, V. Kumar, A fast and high quality multilevel scheme for partitioning irregular graphs, SIAM J. Sci. Comput. 20 (1) (1998) 359–392.

[14] J. Katz, A. Plotkin, Low Speed Aerodynamics, 2nd Edition, Cambridge University Press, 2001.

[15] J. Kuttenkeuler, M. Carlsson, Optical deformation measurements in wind tunnel testing, in: International Forum on Aeroelasticity and Structural Dynamics, Vol. III, Madrid, 2001, pp. 499–508.

[16] H. Lamb, Hydrodynamics, Dover Publications, 1945.

[17] J.J. Meijer, B.B. Prananta, Static aeroelastic simulation of military aircraft in transonic flow, in: International Forum for Aeroelasticity and Structural Dynamics, Vol. II, Madrid, 2001, pp. 119–132.

[18] S. Modak, E.D. Sotelino, The generalized method for structural dynamics applications, Adv. Eng. Software 33 (2002) 565–575.

[19] N.M. Newmark, A method of computation for structural dynamics, Eng. Mech. Div. 85 (EM3) (1959) 67–94.

[20] A.B. Qualysis, ProReflex, Technical Reference, Sävedalen, Sweden, 1997.

[21] A.K. Slone, K. Pericleous, C. Bailey, M. Cross, Dynamic fluid structure interaction using finite volume unstructured mesh procedures, Computers and Structures 80 (2002) 371–390.

[22] R.J. Zwaan, B.B. Prananta, Fluid-structure interaction in numerical aeroelastic simulation, Nonlin. Mech. 37 (2002) 987–1002.